Nature Communications

https://doi.org/10.1038/s41467-026-68995-z

Article in Press

A spatiotemporal atlas of cerebrovascular development in zebrafish

Received: 24 July 2025

Accepted: 21 January 2026

Cite this article as: Li, X., Ke, S., Wu, C. *et al.* A spatiotemporal atlas of cerebrovascular development in zebrafish. *Nat Commun* (2026). https://doi.org/10.1038/s41467-026-68995-z

Xiaoyu Li, Shanshan Ke, Chengchao Wu, Mei Wu, Yunfei Ren, Zitong Wang, Jialan Tang, Yuying Zheng, Da Mi & Jingjing Zhang

A Spatiotemporal Atlas of Cerebrovascular Development in Zebrafish

Xiaoyu Li[1,#], Shanshan Ke[1,#], Chengchao Wu[1,#], Mei Wu[1,#], Yunfei Ren[1], Zitong Wang[1], Jialan Tang[1], Yuying Zheng[1], Da Mi[2], Jingjing Zhang[1,3*]

[1]Zhanjiang Key Laboratory of Zebrafish Model for Development and Disease, Affiliated Hospital of Guangdong Medical University, Zhanjiang 524001, China

[2]State Key Laboratory of Membrane Biology, Tsinghua-Peking Center for Life Sciences, IDG/McGovern Institute for Brain Research, School of Life Sciences, Tsinghua University, Beijing 100084, China

[3]School of Medical Technology, Guangdong Medical University, Dongguan 523808, China

[#]These authors contributed equally to this work.

[*]Correspondence: jingjing.zhang@live.com (J Zhang)

Abstract

The vertebrate brain requires precisely patterned vasculature, yet the molecular and cellular dynamics of cerebrovascular development remain incompletely understood. While single-cell studies have profiled brain vasculature, integrating these data across molecular, cellular and architectural scales remains challenging. We combine *in situ* sequencing, single-cell transcriptomics and 3D vascular reconstruction to map zebrafish brain endothelial development (3-11 dpf). Quantitative 3D analysis reveals a developmental shift from lateral vascularization to intraparenchymal angiogenesis, coinciding with blood-brain barrier (BBB) maturation. We identify 6 endothelial subtypes with conserved mammalian signatures, showing capillary endothelial cells (CapECs), the predominant intracranial subtype exhibiting stage-specific enrichment of transporter and tight junction modules. Spatial transcriptomics show progressive CapEC enrichment in mesencephalic/metencephalic regions versus arterial EC accumulation in prosencephalic vessels. Functional assays confirm BBB competency by 11 dpf, while genetic perturbation of three uncharacterized CapEC-enriched genes (*slc16a1a, zgc:158423, cldc1*) disrupts vascular patterning and BBB integrity. This multidimensional atlas provides an evolutionary perspective on cerebrovascular development, bridges molecular profiles with vascular architecture, and offers insights into developmental dynamics across scales.

Keywords: cerebrovascular development; endothelial cells; 3D cerebrovascular network; spatiotemporal transcriptomes; zebrafish

Introduction

The maintenance of cerebrovascular structural and functional integrity constitutes a fundamental pillar of cerebral homeostasis [1]. Dysregulation of cerebrovascular development contributes to the pathogenesis of diverse neurological and cerebrovascular pathologies, such as Alzheimer's disease, vascular dementia, capillary telangiectasias, arteriovenous malformations, and cerebral cavernous malformations [2]. Consequently, a comprehensive understanding of cerebrovascular architecture, cellular dynamics, and molecular properties is essential for deciphering the pathophysiology of neurovascular diseases.

For the past decades, diverse methodologies have emerged for drawing the brain vascular graph, ranging from vascular corrosion casting and dye filling to transgenic vessel labelling and, more recently, lectin labelling combined with tissue clearing [3-6]. Through immunolabeling, advanced tissue clearing, and optimized vasculature segmentation, the adult mouse cerebrovascular network has been comprehensively reconstructed, enabling systematic analysis of whole-brain vascular properties [7]. Beyond structure visualization, deep learning-based vessel segmentation has been employed to distinguish and quantify brain angio-architecture, facilitating detailed analysis of vascular alterations in neurovascular diseases [8-10]. Despite these advances, the structural characteristics of the developing cerebrovasculature during the early developmental stage remain largely unexplored.

Recent advances in single-cell sequencing have enabled unprecedented resolution in decoding the cellular and molecular mechanisms governing brain vasculature [11-15]. Utilizing single-nucleus RNA-seq (snRNA-seq) on *ex vivo* and post-mortem human brain tissue, the characteristics and new cell-type-specific markers of endothelial, mural, and perivascular cells were uncovered [16]. Single-cell RNA-seq (scRNA-seq) analysis of endothelial and mural cells from the prenatal human brain has elucidated the transcriptomic and functional diversity of vascular cells during the second trimester [17]. Furthermore, comparative scRNA-seq studies across human fetal and adult stages, as well as various vascular-related diseases, have mapped the molecular heterogeneity characterizing

brain vascular cells across life stages and pathological contexts [2]. In addition, scRNA-seq revealed region-specific functional heterogeneity of the blood-brain barrier (BBB) between the mouse cortex and median eminence, with distinct molecular signatures underpinning this spatial divergence [18]. However, despite these significant strides, the relationship between the inherent molecular signatures of cerebrovascular cells and their precise anatomical positioning within the brain remains poorly characterized.

Within the brain vasculature, capillaries serve as the most critical component as they constitute the BBB, which regulates the exchange of compounds between the brain and the blood while safeguarding the brain against harmful substances in the bloodstream [19]. Several key endothelial-enriched genes are highly expressed in capillaries, including *Glut1*, *Cldn5*, and *Mfsd2a*, being functionally linked to BBB integrity [20]. Notwithstanding progress in comprehending the molecular mechanisms regulating vascular development, the cellular and molecular attributes of capillary formation and maturation remain enigmatic. Hence, there is considerable interest in unraveling the molecular signatures of capillary development, which could facilitate the identification of novel drug delivery targets to enhance therapeutic efficacy.

The zebrafish model offers an exceptional avenue for uncovering brain vascular development mechanisms due to its remarkable evolutionary conservation with mammals in cerebrovascular structure, function, and molecular regulation, as well as its optically transparent embryos for high-resolution cerebrovascular imaging [21,22]. Crucially, the brain endothelium serves as the anatomical foundation of cerebrovascular, playing a pivotal role in maintaining neurovascular equilibrium and governing cerebral blood flow. To elucidate the vascular, cellular, and molecular characteristics of brain vasculature during the early developmental stage, we leveraged an endothelial-specific transgenic zebrafish line to reconstruct three-dimensional (3D) cerebrovascular architectures across 3 days post-fertilization (dpf), 6 dpf, and 11 dpf. Complementing this structural analysis, we performed scRNA-seq of brain vascular endothelial cells (ECs) at 3, 6, and 11 dpf, systematically investigating gene expression profiles across endothelial subtypes. Finally, integrating these datasets, we established a spatiotemporally resolved transcriptome atlas aligned

with 3D vascular anatomy, revealing stage-specific molecular signatures governing cerebrovascular maturation. Notably, leveraging our comprehensive dataset, we identified the critical roles of capillary-specific genes *zgc:158423, slc16a1a,* and *cldc1* for BBB integrity. Our dataset furnishes a valuable resource for elucidating the integrated vascular, cellular, and molecular networks underlying cerebrovascular development.

Results

3D cerebrovascular network of zebrafish from embryo to larva

To systematically investigate the spatiotemporal characteristics of zebrafish vasculature in the developing brain, we first generated the 3D cerebrovascular atlas spanning embryonic to larval stages (3, 6, and 11 dpf [23,24], **Figure 1A**). We performed confocal imaging with the EC-specific transgenic zebrafish line of *Tg(kdrl:eGFP)*^{s843} and then reconstructed the cerebrovascular network using Imaris. Similar to mammals, the zebrafish brain is perfused via the circle of Willis (COW), which is supplied by the caudal division of the internal carotid artery (CaDI). Blood then distributes to the parenchyma of the prosencephalon, mesencephalon, and metencephalon. For further quantitative analysis, the cerebrovascular architecture was subdivided into lateral, dorsal, ventral, and intraparenchymal subnetworks (**Figure 1A**), with vascular anatomical nomenclature primarily following previous convention [25] (**Table S1**).

3D reconstruction of the developmental zebrafish cerebrovasculature uncovered region-specific dynamic changes in vascular architecture. Quantitative analysis demonstrated significant increases in both vascular length (**Figure 1B**) and segment number (**Figure 1C**), with particularly pronounced angiogenesis observed in five vessels: the prosencephalic communicating vessel (PrCm), middle mesencephalic central artery (MMCtA), medulla oblongata central artery (MoCtA), basilar artery (BA) and nasal vein (NV) (**Figure 1D-E**). These findings indicate robust intraparenchymal vascular expansion during this developmental period. Consistent with previous reports that early metencephalic vascularization originates from the sprouting of the primordial

hindbrain channel (PHBC) [22], both the number of PHBC and MoCtA segments increased significantly from 3 to 6 dpf. However, beyond this stage, the number of MoCtA segments continued to rise (69.40 ± 4.925 *vs.* 113.0 ± 10.28, mean ± SEM), whereas PHBC counts remained unchanged (36.80 ± 1.158 *vs.* 32.80 ± 1.463, mean ± SEM). These spatiotemporal transitions suggest a developmental pattern in the zebrafish cerebrovasculature, progressing from lateral to intraparenchymal vascularization.

Characteristics of cerebrovascular EC subtypes

During early development, the cerebrovascular network undergoes regionally vascular enrichment. ECs, serving as both structural units and functional hubs of vasculature, are closely associated with this process. However, the molecular signatures of ECs and their spatial organization within the vascular network have not yet been systematically integrated. To address this gap, we performed scRNA-seq of fluorescence-activated cell sorting (FACS)-purified cerebrovascular ECs at these 3, 6, and 11 dpf (**Figure 1F**), alongside whole-brain spatial transcriptomic profiling using improved *in situ* sequencing (IISS) [26,27] and vascular mapping (**Figure 1G**).

Single-cell transcriptomic profiling has profoundly advanced our characterization of distinct EC types [28]. Firstly, we integrated EC populations from 3, 6, and 11 dpf (**Figure 2A**), which were filtered using four canonical EC markers (*cdh5*, *kdrl*, *pecam1*, and *fli1a*) (**Figure S1**). Following integration, the cell populations were unbiasedly clustered and visualized using Uniform Manifold Approximation and Projection (UMAP). Through cross-referencing differentially expressed genes in each cluster with previously reported marker genes [29,30], we identified six distinct clusters of ECs, including angiogenic ECs (AngECs), mitotic ECs (MECs), lymphatic ECs (LymECs), venous ECs (VECs), arterial ECs (AECs), and capillary ECs (CapECs) (**Figure 2B-C**).

EC subtypes exhibit functional heterogeneity mediated by subtype-specific gene expression profiles. We characterized the top 25 highly expressed genes (HEGs) in six EC subtypes, providing a set of candidate markers for these cell populations (**Figure S2A and Supplementary Data 1**). We then profiled the temporal dynamics of these marker genes across 3, 6, and 11 dpf, uncovering

diverse developmental patterns of distinct EC subtypes (**Figure S2B and Supplementary Data 2**). Notably, AngECs, AECs, and CapECs displayed progressive upregulation of specific gene modules. In contrast, VECs reached peak module expression at 6 dpf, while MECs exhibited reduced expression by 11 dpf. LymECs maintained consistent expression across all three developmental stages (**Figure S2B)**. These findings highlight subtype-specific functional transitions, suggesting dynamic and coordinated regulation of endothelial specialization during cerebrovascular development.

Dynamic expression module of EC subtypes during development

Following the identification of ECs subtype-specific genes, we conducted functional enrichment analysis and categorized significantly enriched pathways according to their biological functions (**Figure 2D**). Pathways involving signal transduction and signaling interactions were broadly enriched across most EC subtypes. In contrast, CapECs uniquely exhibited significant enrichment in substance transport, indicating their specialized role in BBB formation and maintenance. Subsequent validation confirmed marked significant upregulation of key functional modules in CapECs, including ATP-binding cassette (ABC) transporters, solute carrier (SLC) transporters, and tight junction components, compared to other EC subtypes (**Figure 2E-G**).

Within these modules, we analyzed the developmental profiles at 3, 6, and 11 dpf. The expression of transporter-related modules significantly increases from 3 dpf to 6 dpf and remains elevated thereafter, indicating that BBB transport functionality is still immature at the molecular level at 3 dpf (**Figure 2H-I**), aligning with the high BBB leakage at this developmental stage [31]. In comparison, tight junction-associated modules exhibited a distinct developmental trajectory marked by a sharp expression increase at 6 dpf persisting through 11 dpf, indicating functional establishment of tight junctions around 6 dpf (**Figure 2J**), consistent with the previous conclusion [32]. These results indicate that the coordinated activity of these modules regulates the stepwise maturation of the BBB. We further performed permeability assays to assess BBB functionality at 3, 6, and 11 dpf by injecting Evans Blue (961 Da) into the embryonic common cardinal vein.

Quantitative analysis revealed significant tracer extravasation at 3 and 6 dpf, with peak leakage observed at 3 dpf. Since Evans Blue could bind to serum albumin, forming protein complex with a molecular size around 70 kDa [33,34], this indicates an immature BBB function of 3 to 6 dpf zebrafish. By 11 dpf, Evans Blue was robustly confined to the cerebral vasculature (**Figure S3A-B**), demonstrating functional maturation of the BBB.

Conservation of cerebrovascular EC subtypes between mammals and zebrafish

Characterizing EC features during development enables an in-depth investigation of the conservation of cerebrovascular development between mammals and zebrafish. To systematically compare the developmental processes between species, we integrated published scRNA-seq data of human brain ECs (from GW14 to GW18, GW for gestational week) [2] and mouse brain ECs (from E12.5 to E17.5, E for embryonic day) [35], which corresponding to the zebrafish developmental window from 3 to 6 dpf. The HEGs of zebrafish EC populations exhibited conserved expression profiles in mammalian (human/mouse) EC subtypes (**Figure 3A**), with cross-species correlation analysis confirming robust transcriptional conservation across EC subtypes (**Figure S4A-B**). Furthermore, we present the specific functions associated with gene modules of CapECs during developmental progression in human and mouse (**Figure 3B-D**). Interestingly, the expression trends of both the transporter module and tight junction protein module in mammals are consistent with those in zebrafish during development (**Figures 2H-J**). The conservation of ECs, particularly CapECs, during zebrafish development demonstrates the species' strong potential as an alternative model for mammalian vascular research.

Spatiotemporal transcriptome atlas of cerebrovascular EC subtypes

To delineate the spatial characteristics of ECs during vascular development, we integrated scRNA-seq data with IISS information mapped onto a whole-brain vascular network. In this experimental design, a workflow combining 3D imaging *in vivo* of *Tg(kdrl:eGFP)*^{s843} zebrafish with subsequent serial sectioning and IISS was used for spatially mapping the ECs (**Figure 1G, Methods**). Only the zebrafish with entire brain sections and strong eGFP expression were processed for IISS.

During IISS, the 488 nm channel was exclusively allocated for the vascular eGFP fluorescence acquisition. Vascular matching was achieved by adjusting slice views in 3D reconstructions, enabling the location of $eGFP^+$ regions of interest (ROI) in IISS within the whole-brain network (**Figure S5**).

With this design, we systematically profiled the expression of 36 genes specifically associated with CapECs, AECs, VECs, and AngECs in 3, 6, and 11 dpf zebrafish (**Figures 4A and S6-7**). The analysis yielded robust data: at 3 dpf, 28 slices comprising 8,769 cells and 1,970 vascular regions, with 45,993 transcript counts; at 6 dpf, 25 slices with 6,873 cells, 1,258 regions, and 30,919 counts; and at 11 dpf, 25 slices with 5,425 cells, 1,924 regions, and 33,118 counts. These data demonstrate the high efficiency and depth of our spatial transcriptomic profiling. To validate our spatiotemporal transcriptomic data, we selected *slc2a1a* as a representative gene. Comparative analysis revealed a strong concordance between spatial transcriptomics-derived *slc2a1a* expression patterns and *slc2a1a:eGFP* fluorescence distributions in transgenic zebrafish (**Figure S8A**), confirming the reliability of our approach (**Figure S8B-C**).

Through comprehensive classification, we established a spatiotemporal transcriptomic atlas of cerebrovascular EC types (**Figures 4B and S9**). The procedure involved three key steps: firstly, after capturing the IISS data from these serial sections, we used the spatial distribution of the vasculature from the eGFP channel to align the 2D section with its corresponding, pre-acquired *in vivo* 3D cerebrovasculature map from the same animal (**Figure 4B**, left); subsequently, this 2D-3D registration allowed us to transfer the vessel type annotations from the 3D atlas onto the 2D section (**Figure 4B**, middle); finally, based on this precise vascular annotation, we performed statistical analyses of the cellular and gene information from the IISS data for each vessel type (**Figure 4B**, right). This atlas revealed the distribution of four EC subtypes, with CapECs consistently predominating in the vast majority of intracranial vasculature (> 50%, **Figure 4C**). Unlike the majority pattern, the lateral vessels (NV and PMBC) showed progressive CapEC reduction coupled with VEC accumulation during development.

To elucidate the subtype-specific developmental changes in vascular patterning, we mapped the density distributions of individual major EC subtypes (CapEC, AEC, VEC, and AngEC) within our 3D vascular atlas (**Figure 4D**). All subtypes exhibited preferential localization in lateral vasculature (PMBC and PHBC), with progressive developmental enrichment into intraparenchymal vessels of mesencephalon and metencephalon, including the posterior mesencephalic central artery (PMCtA) and medulla oblongata central artery (MoCtA). PrCm displayed an increasing AEC enrichment during 6 and 11 dpf, indicating gradual arterial specialization. In contrast, the cerebellar central artery (CCtA) and metencephalic artery (MtA) maintained weak EC specification throughout all stages, suggesting delayed vascular angiogenesis that may parallel its neurodevelopment (**Figure 4D-E**). Intriguingly, our spatiotemporal transcriptomic atlas exhibited highly concordant distribution patterns among these EC subpopulations. To validate these findings, we implemented amplification-based single molecules *in situ* hybridization (asmFISH) assay, which further verified the co-localization of distinct EC subtypes within the same vascular segments (**Figure S10A-B**). Furthermore, we also detected the cells expressed markers of EC subtypes (**Figure S10C-H**). These findings demonstrate progressive spatiotemporal specialization of EC properties in the developing zebrafish cerebrovasculature from embryonic to larval stages.

Functional evaluation of genes enriched in CapECs

During cerebrovascular development, the BBB emerges as a highly specialized functional interface. Here, we focused on CapECs as they constitute the pivotal cellular component responsible for BBB functionality. Leveraging our spatiotemporal transcriptomic dataset, we found that several genes enriched in CapECs relative to other EC subtypes upon isolation (*cldn5a*, *lef1,* and *fabp11a*, et.al) have been investigated to be associated with BBB [36,37]. Fortunately, we also identified three uncharacterized zebrafish capillary high expression genes including *zgc:158423*, *slc16a1a,* and *si:ch73-86n18.1* (also known as *cldc1*) in our scRNA-seq (**Figure S11A**). Through *in situ* hybridization in zebrafish embryos, we verified their specific expression within the cerebrovasculature (**Figure S11B**).

Both *slc16a1a* (orthologous to mouse *Slc16a1* and human *SLC16A1*) and *zgc:158423* (conserved with mouse *Slc3a2* and human *SLC3A2*) have been reported as transporters located at the BBB [38,39], whereas their functions in BBB development remain undefined. We analyzed the density distribution of *slc16a1a*$^{+}$ ECs and *zgc:158423*$^{+}$ ECs using our spatiotemporal transcriptome atlas (**Figure 5A-B**). At 3 dpf, both EC populations were primarily distributed in the lateral PHBC and PMBC, followed by the AMCtA, MMCtA, PMCtA in mesencephalon, and the MoCtA in metencephalon. During subsequent development, these ECs gradually enriched in the major mesencephalon and metencephalon vessels, exhibiting spatial distribution characteristics similar to those of CapECs in spatial transcriptomics.

To investigate the functions of *slc16a1a*, *zgc:158423*, and *cldc1*, we generated corresponding crispants in zebrafish using CRISPR/Cas9 technology (**Figures 5C and S12A**). At 3 dpf, both *slc16a1a* and *zgc:158423* crispants exhibited comparable vascular defects, including significant reductions in total vessel length and segment number, predominantly in the mesencephalic region (**Figure 5C-G**). By 6 dpf, only a subset of vessels in *slc16a1a* crispants displayed impairments in length or segment number (**Figure S12A-E**). In contrast, *cldc1* crispants showed no obvious vascular abnormalities at 3 dpf; however, a significant decrease in vascular length and segment number was detected by 6 dpf (**Figures 5C-G and S12A-E**). We also calculated vascular straightness and found no substantial difference between the crispants and the controls (**Figure S12F-I**). Notably, *cldc1* crispants also showed a high hemorrhage rate in the cerebral vasculature at 3 dpf, indicating its essential role in cerebrovascular stability (**Figure S11C**). We next assessed BBB permeability in the crispants. Evans Blue leakage assays revealed significantly increased extravasation in both *slc16a1a* and *zgc:158423* crispants at 3 dpf, which persisted through 6 dpf (**Figure 5H-K**). In contrast, *cldc1* crispants exhibited no leakage at either time point, confirming intact BBB integrity.

Moreover, we performed morpholino oligonucleotide (MO)-mediated knockdown of *zgc:158423* and *slc16a1a*. The morphants recapitulated the vascular defects observed in crispants. At 3 dpf, both morphants showed significant reductions in vessel length in the PrCm, AMCtA, CCtA, and

MoCtA regions (**Figure S13A-E)**. By 6 dpf, these vascular defects were attenuated, consistent with the phenotype seen in crispants (**Figure S13F-J**). BBB assessment in morphants also revealed permeability defects consistent with those in crispants **(Figure S14)**. Collectively, the vascular abnormalities and increased permeability observed in both *slc16a1a* and *zgc:158423* crispants and morphants underscore the critical roles of these genes in zebrafish cerebrovascular development and BBB integrity.

In summary, through integrating single-cell transcriptomics, spatial transcriptomics, and 3D vascular reconstruction, we delineate the molecular characteristics and spatial distribution patterns of EC subtypes during the early development of zebrafish cerebrovasculature. This work establishes both a comprehensive molecular atlas of cerebrovascular ECs and a multidimensional analytical framework for investigating cerebrovascular development and related pathologies.

Discussion

In this study, we constructed a spatiotemporal transcriptomic atlas of zebrafish cerebrovascular development by integrating 3D vascular network mapping with single-cell profiling. This approach yielded several key findings, including the dynamic cerebrovascular structure characteristics and EC subtype-specific molecular features from embryonic to larva stages, the evolutionary conservation of these spatiotemporal patterns, the dominant role of CapECs in developing intracranial vasculature, and the critical functions of several representative capillary-specific genes (*slc16a1a, zgc:158423,* and *cldc1*) in regulating vascular development and BBB integrity.

Research on whole-brain vascular structure is of great significance for understanding the pathology of aberrant cerebrovascular development, cerebrovascular diseases, and neurological disorders [7,40-42]. However, due to the *in-utero* development of mouse embryos, the establishment pattern of early-stage cerebrovascular networks remains elusive. Previous studies have mapped embryonic cerebrovascular networks using zebrafish [43]. Here, to further characterize early cerebrovascular

development, we reconstructed a 3D atlas of the zebrafish cerebrovascular network spanning embryonic to larval stages. The foundational studies[25] established a critical 2D anatomical framework, which inspired us to extend this work by introducing a quantitative, 3D perspective. Quantitative analysis revealed region-specific developmental patterns, extensive vascular remodeling occurs in the midbrain and hindbrain from 3 dpf to 11 dpf, whereas forebrain vasculature remains largely stable from 3 dpf to 6 dpf but exhibits significant growth at 11 dpf. It remains to be further investigated whether the cerebrovasculature of early-stage mice undergoes similar network remodeling. Moreover, reconstructing specific brain vascular regions in juvenile and adult zebrafish via tissue clearing and light-sheet imaging [44,45], followed by comparative analysis with their early-stage counterparts, including the specialization of the midbrain MMCtA and the establishment of cerebrovascular networks in the cerebrum and cerebellum, will fundamentally advance our understanding of network construction across the entire developmental continuum. In addition, the atlas will provide a reference framework for developing machine learning pipelines to automatically quantify zebrafish vascular development, enabling systematic analysis of pathological vasculature in models of cerebrovascular disease.

The observation of significant regional differences during early cerebrovascular development prompted us to further investigate their underlying cellular basis. We conducted scRNA-seq on brain endothelial cells across these three developmental stages and found no distinct subpopulations emerging over these time points. Consequently, we further explored how the spatial positioning of endothelial cells contributes to regional specificity. Over the past decades, a series of spatial transcriptomics technologies have been developed to gain a comprehensive understanding of cellular spatial organization (e.g., seqFISH+, MERFISH, Single-cell Stereo-seq, DBiT-seq, *in situ* sequencing) [46-50]. Utilizing stereo-seq has revealed spatial developmental trajectories during zebrafish embryogenesis [51], whereas the compact structure of the zebrafish brain necessitates higher cellular resolution to resolve cerebrovascular development. To precisely map the spatial dynamics of cerebrovascular ECs, we integrated the IISS with reconstructed 3D vascular networks and generated a high-resolution developmental atlas of EC subtype (AngECs,

VECs, AECs, and CapECs) topography across embryonic-to-larval zebrafish cerebrovasculature. Regarding its specific advantages for cerebral vasculature research, IISS is uniquely powerful. First, its high sensitivity and specificity, achieved via rolling circle amplification (RCA), are crucial for detecting lowly expressed regulatory genes within the sparse endothelial cell population. Second, its customizable gene panel allows us to focus precisely on endothelial-specific and developmentally relevant targets. Most importantly, IISS provides single-cell resolution while perfectly preserving tissue morphology. This is indispensable for unambiguously assigning transcriptional identities to specific vessel types (e.g., arteries, capillaries, veins) within the complex, intricate architecture of the developing brain, which is simply not possible with bulk or dissociated single-cell methods.

Although the relative proportions of gene-specific EC subtypes remained stable across regions and stages, we detected pronounced spatiotemporal variations in EC density during development, which may underline regional differences in cerebrovascular growth. In addition, cerebrovascular development is not solely directed by endothelial cells but involves integral contributions from other components of the neurovascular unit, including pericytes, neurons, and astrocytes [52,53]. How brain ECs dynamically interface with these partners to modulate cerebrovascular development requires further exploration.

Notably, we observed the coexistence of four distinct EC subtypes within individual vascular segments, with CapECs predominating in intracranial vessels, including structures previously classified as central arteries. Considering that early developmental intracranial vasculature in zebrafish consists exclusively of microvessels (exhibiting significantly smaller diameters compared to dorsal vessels and primitive conduits), we therefore speculated that CapECs' predominance represents an inherent developmental program in zebrafish cerebral vascular patterning.

Moreover, single-cell analysis of zebrafish brain vasculature at 3, 6, and 11 dpf resolved 6 EC subpopulations: AngECs, MECs, LymECs, VECs, AECs, and CapECs. By contrast, previous

vascular analyses of prenatal human brains have identified five distinct EC subtypes, including tip cells, mitotic cells, capillary cells, arterial cells, and venous cells [17]. Integrative analysis of human fetal, adult, and diseased cerebrovasculature reveals 14 major EC subpopulations, including proliferating cells, arteries, venules, capillaries, and angiogenic capillaries [2]. We speculate that the zebrafish AngECs subgroup might be functionally mirror human tip cells or angiogenic capillaries, which exhibit mixed properties of MECs and CapECs. Furthermore, we demonstrate remarkable conservation of EC properties between zebrafish and mammals, suggesting a fundamental conservation of brain endothelial cell types between zebrafish and mammals, highlighting the utility of zebrafish as a model for interrogating vascular mechanisms that are challenging to study in mammalian systems.

Since both *zgc:158423* and *slc16a1a* were linked to BBB integrity, we hypothesized that their human orthologs might be involved in cerebrovascular or neurodegenerative disorders. To test this hypothesis, we analyzed associations in public GWAS datasets encompassing two disease categories: 8 cerebrovascular diseases and 5 neurodegenerative disorders (**Figure S15**). The results revealed a possible association between cerebral infarction and *SLC16A1*, as well as links between two neurodegenerative diseases (dementia and epilepsy) and *SLC3A2*. These findings imply potential roles for both genes in the pathogenesis of the aforementioned disorders.

This study demonstrates the utility of the zebrafish as a conserved model for cerebrovascular development, providing a powerful alternative system for investigating human cerebrovascular development and associated pathologies. Based on our established cerebrovascular transcriptomic mapping pipeline, future studies could encompass all cellular components of the neurovascular unit. Systematically resolving their spatial architecture and molecular crosstalk will illuminate fundamental mechanisms governing cerebrovascular development, aging dynamics, and disease pathogenesis.

Methods

Fish lines and maintenance

Zebrafish (*Danio rerio*) were raised and maintained following the standard procedure in ZFIN (http://zfin.org) in accordance with the Guangdong Provincial Regulations on the Administration of Laboratory Animals, under rigorous oversight by the animal ethics committee of Guangdong Medical University. Zebrafish at 3, 6, and 11 dpf from the *Tg(kdrl:eGFP)*^{s843} [54], *Tg(kdrl:ras-Cherry)*^{s916} [55] and *Tg(slc2a1a:eGFP)* (a gift from Dr. Dong Liu's laboratory, Nantong University, China) zebrafish line were used in this study, in which sex is not yet determined at these developmental stages.

3D imaging and vascular reconstruction

3D imaging of zebrafish embryos was performed using the confocal laser scanning microscope Nikon AX (Nikon, Japan) with a 10× objective (zoom 1.6-2.0). To facilitate 3D reconstruction, optical sections were acquired at 1 μm z-intervals with the pinhole adjusted to 0.4 Airy units. Zebrafish were treated with 1-phenyl 2-thiourea (PTU, 0.03 g/L) from 10 hours post-fertilization to prevent pigmentation. Before imaging, the transgenic zebrafish were anesthetized with 0.03% tricaine (Sigma-Aldrich) and mounted in 1% low-melting point agarose (LMA, Sigma-Aldrich) in a confocal dish with ventral side up. After imaging, the surface and filaments modules of Imaris 10.2.0 (Oxford Instruments, UK) were used for vascular reconstruction. The segment length and number of connected vasculatures were quantified. The vessel nomenclature follows established literature [25], with modified abbreviations for clearer brain region representation (**Table S1**).

scRNA-seq of zebrafish brain ECs

At 3, 6, and 11 dpf, zebrafish were anesthetized in the E3 medium, and brain tissues were isolated within 30 min. 1500-2000 brain tissues were isolated from the above zebrafish at the corresponding time point and incubated at 37°C with tissue digestion solution containing 2 mg/L of papain (9001-73-4, Sigma-Aldrich) for about 25 min. Then the tissues were incubated with Dulbecco's Modified

Eagle Medium (DMEM) medium containing 5% fetal bovine serum (FBS) to terminate the digestion. Cell suspensions were centrifuged at 500 g for 30 min at 4°C and resuspended in DMEM medium containing 5% FBS. Then cell suspensions were filtered through the 70 μm, 40 μm cell strainers to prepare single-cell suspensions. All filtration procedures were performed on ice to preserve cell viability. eGFP-positive cells were sorted by FACS Aria II and collected with DMEM medium containing 5% FBS. After centrifugation of sorted cells, the cells were resuspended in DMEM medium with 5% FBS to obtain the appropriate cell density. Samples with more than 80% viable cells were labeled with barcodes. Then, sequencing libraries were constructed using Chromium Next GEM Single Cell 3' Reagent Kits v3.1 and sequenced using the Illumina NovaSeq 6000.

Processing of scRNA-seq data

Raw sequencing reads of the samples were generated by the Cell Ranger (v.7.1.0) workflow. Quality control, removing doublets, empty droplets, and cells with higher mitochondrial containment, were performed with the Seurat (v. 4.3.0) package in R (4.3.0). To exclude the contamination of non-ECs, four canonical makers (*cdh5*, *kdrl*, *pecam1*, and *fli1a*) were used to identify the EC clusters. ECs filtered from three data sets were then integrated by the Integrated Data function in Seurat [56]. Then the data were subjected to unsupervised clustering and visualized with t-SNE. The differentially expressed genes were identified by the FindAllMarkers and FindMarkers functions provided by the Seurat package [57]. Functional pathway enrichment analysis on the gene sets was performed by clusterProfiler [58].

Cell conservation analysis

The differentially expressed genes among CapECs, AECs, and VECs were identified by the Find Markers function. Correlation analysis between mammals and zebrafish was performed by the MetaNeighbor package. Mouse and human genes were transferred to their homologous genes of zebrafish by the biomaRt package [59,60]. scRNA-seq of mouse and human cerebrovascular was obtained from previous literature [2,35]. The correspondence of cerebrovascular developmental

stages is as follows: zebrafish (3 dpf to 6 dpf), mouse (E14.5 to E17.5), and human (GW14 to GW18).

Sample preparation for IISS

The live imaging of the 3D brain vascular was conducted as described above. The imaged zebrafish were recovered in the egg water for 2 h, then were fixed at room temperature in the 4% (w/v) paraformaldehyde (PFA) fixed solution for 0.5 h to preserve the vascular eGFP signal. After washing with 1×PBS three times, the head of fixed zebrafish was isolated with Venus scissors. Then the tissue was transferred into the mold, and the excess PBS was removed. OCT was used to embed the zebrafish brain in a supine position, and immediately frozen with dry ice powder. The samples were preserved at -80°C before frozen section. Zebrafish brain tissues were cryosectioned at 10 μm using a freezing microtome (Dakewe, CT520), with collection beginning from the dorsal first tissue slice until the gills appeared. The sections were collected in a 1.5×1.5 cm^2 region on one adhesion microscope slide (CITOTEST, China). To check whether the vascular signal (eGFP) is still retained, these sections were imaged by Mica microscopy (Leica, Germany). To verify whether the blood vessels in the slices were intact, the vasculatures were carefully compared artificially with the 3D vascular network. Only the zebrafish with entire brain sections (without loss, damage, or folding) and strong eGFP expression were processed for IISS.

IISS assay procedure

Before IISS, *ubc* and *dapb* were used as the positive and negative controls, respectively, to detect whether the sections could be used. IISS was performed by Suzhou Dynamic Biosystem Co., Ltd. In detail, sections were first fixed with 4% PFA for 5 min, followed by washing twice with 1×DEPC-PBS and dehydrated with a gradient of ethanol. After being rinsed three times with washing buffer (SEERNA Bioscience, Xiamen, China), permeabilization of the sections was conducted with 0.1 M HCl at 37°C for 5 min. Then the sections were incubated in order with 1) hybridization mix solution containing target probes at 37°C for 4 h; 2) ligation mix at 37°C for 30 min; 3) splicing primers in circulation mix at 37°C for 30 min; 4) rolled circular amplification mix

at 30°C overnight. After completing each of these steps, the sections were washed three times by using the washing buffer at 30°C. Then, sections were incubated with ligation buffer containing anchored primers, labeled probes, and ligases at 30°C following the mounting of sections by utilizing SlowFade Gold Antifade Mountant (Thermo Fisher Scientific, Shanghai, China) that contains 0.5 μg/mL DAPI (Sigma, Shanghai, China). Leica DM6B microscope equipped with DFC9000GT camera was utilized to image with a 20x objective. Following imaging, sequencing primers were eluted with stripping buffer (SEERNA Bioscience, Xiamen, China), and then the sections were washed three times with washing buffer for 5 min. These tissue sections would be reused in the next rounds, until the completion of the whole experimental procedure.

Process of IISS data

Registration of multi-round imaging data

Due to the multiple rounds of imaging in the IISS experiment, images between different rounds would produce displacement, and image registration is necessary. Scale-invariant feature transform algorithm was used to extract the matching feature points between the common reference image and the image to be registered. Then, the change matrix between the two images was calculated according to the relative position relationship between each set of matching feature points. At last, the image was corrected by an affine transformation to achieve image registration.

Cell segmentation

To assign gene signals to cells for downstream analysis, the delineation of cellular spatial boundaries relative to mRNA transcripts is required. First, DAPI images were used to detect nuclei using a deep learning algorithm, cellpose, for cellular segmentation. Then each nucleus was expanded outwards until either 20 pixels max distance was reached or the boundary of another cell was reached. Finally, we have obtained the cell outline coordinates for further analysis.

Vascular localization of cells

The fluorescent signal (eGFP) of blood vessels was also captured in our tissue sections to provide

vascular positional information for cells. To reduce misalignment between multi-channel images, the registration process between DAPI images and eGFP images was performed as follows: using the tissue boundary in DAPI-stained images as a spatial reference, a feature-based rigid registration algorithm was applied to achieve the initial alignment of cross-modal images, ensuring the consistency of tissue structures across different channels. Based on the coarse registration, non-rigid optimization is performed by leveraging the distribution features of eGFP-labeled blood vessels. The optical flow method is used to establish a local deformation field, and sub-pixel-level registration is achieved through mutual information maximization or feature matching optimization, ensuring that the spatial correspondence of blood vessels meets the requirements of subsequent quantitative analysis.

Then, the cerebrovascular segmentation was performed. Morphological transformations are employed to eliminate non-uniform background interference in fluorescence imaging, and high-frequency vascular features are extracted through structural element matching, effectively enhancing the signal-to-noise ratio in low-contrast regions. Initial segmentation is achieved based on a local adaptive threshold algorithm, with the threshold dynamically calculated according to the local regional features of the image. By dynamically computing the statistical characteristics of the pixel neighborhood, a vascular binary mask robust to illumination variations is generated. Optimize the segmentation results based on the distribution of marker labels, remove pseudo-vascular noise, and output a binary image of the vascular network with complete structure.

For spatial matching of cerebrovascular segments, the longer $eGFP^+$ segments served as landmarks to identify the slice in the 3D vascular network (reconstructed from prior 3D imaging of the same fish), with relative positioning guiding vascular annotation in other $eGFP^+$ ROIs. We then calculated the absolute positions of vascular regions and the centroid coordinates of cells to identify intravascular cells and annotate their vascular localization.

Cells whose centroids fell within the vascular regions were classified as vascular cells. These cells were subsequently assigned through the correlation of their transcriptional profiles with scRNA-

seq data. Gene expression of IISS was evaluated at the cellular level. The density distributions of vascular ECs were displayed on the reconstructed 3D cerebrovascular network.

Further analysis of IISS data

To gain the signal position in the images, the watershed algorithm based on local extremum was used to identify and locate the signals in the images. By combining the signal coordinates, cell segment outline, and blood vessel segment information, gene signals were assigned to the cells, and the cells were then assigned to the vascular region. Finally, we obtained the information that included the coordinates of gene signal and cell centroids, the outline of cells and blood vessels, and the matrices of signal-cell and cell-blood vessel.

Amplification-based single-molecule in situ hybridization assays

The RNA amplification-based single-molecule *in situ* hybridization (asmFISH) assays were performed using the SEERNA® FISH RNA Fluorescence *in situ* Hybridization Kit according to the manufacturer's standard protocol [61]. Two sets of probes were used: the *stabl*, *cldn5a*, and *heyl* probes were conjugated with Cy3, Cy3.5, and Cy7 respectively, and the *dab2*, *slc2ala*, and *hey2* probes were correspondingly labeled with Cy3, Cy3.5, and Cy7. All probes were synthesized by Thermo Fisher Scientific.

Whole-mount RNA *in situ* hybridization

The whole mount *in situ* hybridization was performed as previously described [62]. For *zgc:158423*, *slc16a1a*, and *cldc1* probes synthesis, total RNA was extracted from 3 dpf zebrafish and reverse-transcribed into cDNA using Hifair® AdvanceFast 1st Strand cDNA Synthesis Kit (11150ES10, Yeasen, China). Then, target gene sequences were amplified from the aforementioned cDNA by 2× Hieff® PCR Master Mix (With Dye, 10102ES08, Yeasen, China) with the primers listed in Table S2. The PCR products were cloned into the pGM-T vector using the pGM-T Ligation Kit (VT202-01, TIANGEN, China). Then plasmid DNA was isolated from positive clones, and the correct insert sequence was confirmed by Sanger sequencing. The verified plasmids were

linearized by digestion with NdeI and antisense RNA probes were synthesized by in vitro transcription using the T7 RNA polymerase with the linearized plasmids as templates. Images were captured by Leica stereomicroscope (M205).

Generation of crispants by CRISPR/Cas9

The gRNA target sites were designed using CRISPOR (https://crispor.gi.ucsc.edu/), and those with high specificity score and predicted efficiency were selected for synthesized by Tsingke (**Table S3**). For microinjection, the ribonucleoprotein (RNP) complex was prepared by mixing 600 ng of Cas9 protein (M0646T, NEB) with 800 ng of each sgRNA in a 2 μL reaction system (consisting of 0.2 μL Cas9 mRNA [3000 ng/μL stock], 0.8 μL sgRNA1 [1000 ng/μL stock], 0.8 μL sgRNA2 [1000 ng/μL stock] and 0.2 μL 10×buffer). Subsequently, 2 nL of the RNP mixture was injected into one-cell stage *Tg*(*kdrl:eGFP)*^{s843} zebrafish embryos. Control embryos were injected with an equivalent amount of Cas9 protein. The mutagenesis efficiency was evaluated at 1 dpf using the T7 Endonuclease I (T7E1) followed by sequencing. The primers for mutagenesis efficiency detection were listed in **Table S2.**

Morpholino (MO) injection

Translation blocking MOs were designed and synthesized by Gene Tools, LLC. The MO sequences used were *zgc:158423* (5'-*CAGTTCTATGTCCTTCATTTCTCCT*-3') and *slc16a1a* (5'-*CATGGCTCCAGGTGTTTACAAACCA*-3'). 0.5 ng of *zgc:158423* and 2.5 ng of *slc16a1a* MO were injected into the *Tg(kdrl:eGFP)*^{s843} embryos yolk at one cell stage, respectively.

Imaging and analysis of cerebrovascular permeability

Evans Blue (961 Da) was injected into the common cardinal vein of zebrafish at 3 and 6 dpf. After 20 minutes of circulation, the brains of anesthetized larvae were imaged using Nikon AX confocal microscopy with dual-channel laser excitation at 488 nm and 561 nm. For leakage quantification, maximum intensity projections of 99 μm thickness were generated by Image J. Extravascular tracer puncta within the brain parenchyma were counted and normalized to the control group.

Gene-disease association analysis

The GWAS summaries were obtained from the Neale lab website (https://www.nealelab.is/uk-biobank). The association was defined as the distances from significant risk SNPs to the transcriptional start site (TSS) of genes. The significance threshold for risk-associated SNPs was set at $p < 5 \times 10^{-8}$. Disease selection was based on the ICD-10 classification system.

Statistical analysis

Statistical tests were conducted in the R statistical computing environment (R Core Team, 2023). Unpaired two-tailed Student's *t*-test was used to compare the difference between the two experimental groups. The Wilcoxon test was used to assess the difference between two groups with more than 30 samples, such as marker genes identified by FindMarkers and FindAllMarkers. Kruskal-Wallis test with Dunn's multiple comparisons was used to compare the differences among 3, 6, and 11 dpf. p value < 0.05 was considered statistically significant, *$p < 0.05$, **$p < 0.01$, ***$p < 0.001$, ****$p < 0.0001$.

Data availability

The data that support the findings of this study have been deposited into NCBI Gene Expression Omnibus (GEO) database with the accession number of "GSE243907" (https://www.ncbi.nlm.nih.gov/geo/query/acc.cgi?acc= GSE243907).

Code availability

We have uploaded all the research codes in the GitHub repository (https://github.com/lixy0323/cerebrovascular-atlas).

Reference

1. Profaci, C.P., Munji, R.N., Pulido, R.S. & Daneman, R. The blood-brain barrier in health and disease: Important unanswered questions. *J Exp Med* **217**(2020).

2. Wälchli, T. *et al.* Single-cell atlas of the human brain vasculature across development, adulthood and disease. *Nature* **632**, 603-613 (2024).

3. Quintana, D.D. *et al.* The cerebral angiome: High resolution MicroCT imaging of the whole brain cerebrovasculature in female and male mice. *Neuroimage* **202**, 116109 (2019).

4. Lugo-Hernandez, E. *et al.* 3D visualization and quantification of microvessels in the whole ischemic mouse brain using solvent-based clearing and light sheet microscopy. *J Cereb Blood Flow Metab* **37**, 3355-3367 (2017).

5. Di Giovanna, A.P. *et al.* Whole-Brain Vasculature Reconstruction at the Single Capillary Level. *Sci Rep* **8**, 12573 (2018).

6. Zhang, L.Y. *et al.* CLARITY for High-resolution Imaging and Quantification of Vasculature in the Whole Mouse Brain. *Aging Dis* **9**, 262-272 (2018).

7. Kirst, C. *et al.* Mapping the Fine-Scale Organization and Plasticity of the Brain Vasculature. *Cell* **180**, 780-795.e25 (2020).

8. Todorov, M.I. *et al.* Machine learning analysis of whole mouse brain vasculature. *Nat Methods* **17**, 442-449 (2020).

9. Li, Y. *et al.* A high-performance deep-learning-based pipeline for whole-brain vasculature segmentation at the capillary resolution. *Bioinformatics* **39**(2023).

10. Guo, B. *et al.* Self-supervised learning for accurately modelling hierarchical evolutionary patterns of cerebrovasculature. *Nat Commun* **15**, 9235 (2024).

11. Sabbagh, M.F. *et al.* Transcriptional and epigenomic landscapes of CNS and non-CNS vascular endothelial cells. *Elife* **7**(2018).

12. Hupe, M. *et al.* Gene expression profiles of brain endothelial cells during embryonic development at bulk and single-cell levels. *Sci Signal* **10**(2017).

13. Vanlandewijck, M. *et al.* A molecular atlas of cell types and zonation in the brain vasculature. *Nature* **554**, 475-480 (2018).

14. Yang, A.C. *et al.* A human brain vascular atlas reveals diverse mediators of Alzheimer's risk. *Nature* **603**, 885-892 (2022).

15. Wälchli, T. *et al.* Shaping the brain vasculature in development and disease in the single-cell era. *Nat Rev Neurosci* **24**, 271-298 (2023).

16. Garcia, F.J. *et al.* Single-cell dissection of the human brain vasculature. *Nature* **603**, 893-899 (2022).

17. Crouch, E.E. *et al.* Ensembles of endothelial and mural cells promote angiogenesis in prenatal human brain. *Cell* **185**, 3753-3769.e18 (2022).

18. Pfau, S.J. *et al.* Characteristics of blood-brain barrier heterogeneity between brain regions revealed by profiling vascular and perivascular cells. *Nat Neurosci* **27**, 1892-1903 (2024).

19. Benz, F. & Liebner, S. Structure and Function of the Blood-Brain Barrier (BBB). *Handb Exp Pharmacol* **273**, 3-31 (2022).

20. Ben-Zvi, A. *et al.* Mfsd2a is critical for the formation and function of the blood-brain barrier. *Nature* **509**, 507-11 (2014).

21. Gupta, A., Rarick, K.R. & Ramchandran, R. Established, New and Emerging Concepts in Brain Vascular Development. *Front Physiol* **12**, 636736 (2021).

22. Quiñonez-Silvero, C., Hübner, K. & Herzog, W. Development of the brain vasculature and the blood-brain barrier in zebrafish. *Dev Biol* **457**, 181-190 (2020).

23. Jeong, J.-Y. *et al.* Functional and developmental analysis of the blood–brain barrier in zebrafish. *Brain research bulletin* **75**, 619-628 (2008).

24. Quiñonez-Silvero, C., Hübner, K. & Herzog, W. Development of the brain vasculature and the blood-brain barrier in zebrafish. *Developmental biology* **457**, 181-190 (2020).

25. Isogai, S., Horiguchi, M. & Weinstein, B.M. The vascular anatomy of the developing zebrafish: an atlas of embryonic and early larval development. *Dev Biol* **230**, 278-301 (2001).

26. Tang, X. *et al.* Improved in situ sequencing for high-resolution targeted spatial transcriptomic analysis in tissue sections. *J Genet Genomics* **50**, 652-660 (2023).

27. Yu, Y. *et al.* Interneuron origin and molecular diversity in the human fetal brain. *Nat Neurosci* **24**, 1745-1756 (2021).

28. Karlsson, M. *et al.* A single-cell type transcriptomics map of human tissues. *Sci Adv* **7**(2021).

29. Grimm, L. *et al.* Single-cell analysis of lymphatic endothelial cell fate specification and differentiation during zebrafish development. *Embo j* **42**, e112590 (2023).

30. Trimm, E. & Red-Horse, K. Vascular endothelial cell development and diversity. *Nat Rev Cardiol* **20**, 197-210 (2023).

31. O'Brown, N.M., Megason, S.G. & Gu, C. Suppression of transcytosis regulates zebrafish blood-brain barrier function. *Elife* **8**(2019).

32. Xie, J., Farage, E., Sugimoto, M. & Anand-Apte, B. A novel transgenic zebrafish model for blood-brain and blood-retinal barrier development. *BMC Dev Biol* **10**, 76 (2010).

33. Fleming, A., Diekmann, H. & Goldsmith, P. Functional characterisation of the maturation of the blood-brain barrier in larval zebrafish. *PloS one* **8**, e77548 (2013).

34. Patterson, C.E., Rhoades, R.A. & Garcia, J. Evans blue dye as a marker of albumin clearance in cultured endothelial monolayer and isolated lung. *Journal of applied physiology* **72**, 865-873 (1992).

35. La Manno, G. *et al.* Molecular architecture of the developing mouse brain. *Nature* **596**, 92-96 (2021).

36. Zhang, J. *et al.* Fatty Acid Binding Protein 11a Is Required for Brain Vessel Integrity in Zebrafish. *Front Physiol* **8**, 214 (2017).

37. Roudnicky, F. *et al.* Identification of a combination of transcription factors that synergistically increases endothelial cell barrier resistance. *Sci Rep* **10**, 3886 (2020).

38. Bay, C. *et al.* Functional Characterization of the Solute Carrier LAT-1 (SLC7A5/SLC2A3) in Human Brain Capillary Endothelial Cells with Rapid UPLC-MS/MS Quantification of Intracellular Isotopically Labelled L-Leucine. *Int J Mol Sci* **23**(2022).

39. Soares, R.V., Do, T.M., Mabondzo, A., Pons, G. & Chhun, S. Ontogeny of ABC and SLC transporters in the microvessels of developing rat brain. *Fundam Clin Pharmacol* **30**, 107-16 (2016).

40. Zhang, X. *et al.* High-resolution mapping of brain vasculature and its impairment in the hippocampus of Alzheimer's disease mice. *Natl Sci Rev* **6**, 1223-1238 (2019).

41. Sweeney, M.D., Kisler, K., Montagne, A., Toga, A.W. & Zlokovic, B.V. The role of brain vasculature in neurodegenerative disorders. *Nat Neurosci* **21**, 1318-1331 (2018).

42. Winkler, E.A. *et al.* A single-cell atlas of the normal and malformed human brain vasculature. *Science* **375**, eabi7377 (2022).

43. Park, O.K. *et al.* 3D Light-Sheet Fluorescence Microscopy of Cranial Neurons and Vasculature during Zebrafish Embryogenesis. *Mol Cells* **38**, 975-81 (2015).

44. Pende, M. *et al.* A versatile depigmentation, clearing, and labeling method for exploring nervous system diversity. *Sci Adv* **6**, eaba0365 (2020).

45. Susaki, E.A. *et al.* Whole-brain imaging with single-cell resolution using chemical cocktails and computational analysis. *Cell* **157**, 726-39 (2014).

46. Eng, C.L. *et al.* Transcriptome-scale super-resolved imaging in tissues by RNA seqFISH. *Nature* **568**, 235-239 (2019).

47. Chen, K.H., Boettiger, A.N., Moffitt, J.R., Wang, S. & Zhuang, X. RNA imaging. Spatially resolved, highly multiplexed RNA profiling in single cells. *Science* **348**, aaa6090 (2015).

48. Wei, X. *et al.* Single-cell Stereo-seq reveals induced progenitor cells involved in axolotl brain regeneration. *Science* **377**, eabp9444 (2022).

49. Liu, Y. *et al.* High-Spatial-Resolution Multi-Omics Sequencing via Deterministic Barcoding in Tissue. *Cell* **183**, 1665-1681.e18 (2020).

50. Ke, R. *et al.* In situ sequencing for RNA analysis in preserved tissue and cells. *Nat Methods* **10**, 857-60

(2013).

51. Liu, C. *et al.* Spatiotemporal mapping of gene expression landscapes and developmental trajectories during zebrafish embryogenesis. *Dev Cell* **57**, 1284-1298.e5 (2022).

52. Zhao, Z., Nelson, A.R., Betsholtz, C. & Zlokovic, B.V. Establishment and Dysfunction of the Blood-Brain Barrier. *Cell* **163**, 1064-1078 (2015).

53. Schaeffer, S. & Iadecola, C. Revisiting the neurovascular unit. *Nat Neurosci* **24**, 1198-1209 (2021).

54. Jin, S.-W., Beis, D., Mitchell, T., Chen, J.-N. & Stainier, D.Y. Cellular and molecular analyses of vascular tube and lumen formation in zebrafish. (2005).

55. Cross, L.M., Cook, M.A., Lin, S., Chen, J.-N. & Rubinstein, A.L. Rapid analysis of angiogenesis drugs in a live fluorescent zebrafish assay. *Arteriosclerosis, thrombosis, and vascular biology* **23**, 911-912 (2003).

56. Hao, Y. *et al.* Integrated analysis of multimodal single-cell data. *Cell* **184**, 3573-3587.e29 (2021).

57. Satija, R., Farrell, J.A., Gennert, D., Schier, A.F. & Regev, A. Spatial reconstruction of single-cell gene expression data. *Nat Biotechnol* **33**, 495-502 (2015).

58. Xu, S. *et al.* Using clusterProfiler to characterize multiomics data. *Nat Protoc* **19**, 3292-3320 (2024).

59. Durinck, S., Spellman, P.T., Birney, E. & Huber, W. Mapping identifiers for the integration of genomic datasets with the R/Bioconductor package biomaRt. *Nat Protoc* **4**, 1184-91 (2009).

60. Durinck, S. *et al.* BioMart and Bioconductor: a powerful link between biological databases and microarray data analysis. *Bioinformatics* **21**, 3439-40 (2005).

61. Lin, C. *et al.* Imaging of individual transcripts by amplification-based single-molecule fluorescence in situ hybridization. *New Biotechnology* **61**, 116-123 (2021).

62. Gan, D., Wu, S., Chen, B. & Zhang, J. Application of the Zebrafish Traumatic Brain Injury Model in Assessing Cerebral Inflammation. *Zebrafish* **17**, 73-82 (2020).

Acknowledgements

We thank Yuezhuang Zheng and Qiumei Hong for expert technical assistance with the zebrafish facility. We also thank Chunbao Liang, Enyu Huang, and Dr. Lianyan Li for scientific discussion and technical support on this project. We thank Dr. Dong Liu for kindly sharing the *Tg*(*slc2a1a:eGFP*) zebrafish line. This work is supported by the National Natural Science Foundation of China (No. 32222028, 32470889), the National Key R&D Program of China (2024YFA1802200, 2024YFA1802600), the High-level Talents Scientific Research Start-up Funds of the Affiliated Hospital of Guangdong Medical University (2081Z20230014, 2081Z20230015), and the Special Project for Clinical and Basic Sci & Tech Innovation of Guangdong Medical University (GDMULCJC2025010, GDMULCJC2024113).

Author Contributions Statement

X.L., C.W., S.K., and J.Z. designed the experiments, analyzed the data, and wrote the manuscript. M.W., X.L., J.T., and Y.Z. performed the experiments and analyzed the data. X.L. and C.W. performed the bioinformatics analysis. Z.W. and Y.R. helped with the imaging and figure preparation. C.W., D.M., and J.Z. discussed and revised the manuscript. J.Z. supervised and designed this project.

Competing Interests Statement

The authors declare no competing interests.

Figure legends

Figure 1. The spatiotemporal decoding strategy of cerebrovascular development in zebrafish

A 3D reconstruction of cerebrovascular networks in zebrafish of *Tg(kdrl:eGFP)*^{s843} at 3, 6, and 11 dpf. Colors encode different vascular subnetworks. Scale bars: 100 μm. **B, C** Quantification of the total length (**B**) and segment number (**C**) of cerebrovasculature in zebrafish at 3, 6, and 11 dpf. N = 5 at each stage. **D-E** Quantification of the length (**D**) and segment number (**E**) of cerebrovascular subnetworks in zebrafish at 3, 6, and 11 dpf. N = 5 at each stage. Red asterisks indicate the vascular subnetworks exhibiting significant differences in both vessel length and segment number. **F-G** Single-cell spatiotemporal transcriptomic profiling strategy for zebrafish cerebrovascular development. Data were presented as mean ± SEM. The Kruskal-Wallis test revealed an overall effect of development stage (shown in the top, ns: no-significant, *$p < 0.05$, **$p < 0.01$, ***$p < 0.001$). Subsequent Dunn's test was applied for post hoc multiple comparisons (showed follow the columns, *p < 0.05, **p < 0.01).

Figure 2. Specific characteristics of six EC subtypes during cerebrovascular development of zebrafish

A UMAP plot demonstrated limited batch effects among the three datasets after integration. **B** UMAP plot of single cells isolated from zebrafish brains with six clusters. AEC, arterial EC; VEC, venous EC; CapEC, capillary EC; AngEC, angiogenesis EC; MEC, mitotic EC; LymEC, lymphoid EC. **C** Dot plot depicting the expression patterns of canonical markers and cell type-specific genes across different EC types. **D** Dot plots showing differential transcription profile of six EC types by gathering important signaling pathways with significant enrichments. Statistical significance was assessed using Chip-Square test. **E-G** Box plots validating the significantly high expression level during cerebrovascular development of ABC transporters (**E,** 49 genes; CapEC: minima: -0.119, maxima: 0.309, median: 0.018, bounds of box: -0.021 to 0.062, and bounds of whiskers: -0.145 to 0.185; AEC: minima: -0.125, maxima: 0.252, median: -0.011, bounds of box: -0.046 to 0.032, and bounds of whiskers: -0.164 to 0.15; AngEC: minima: -0.126, maxima: 0.266, median: -0.032,

bounds of box: -0.059 to -0.001, and bounds of whiskers: -0.147 to 0.087; VEC: minima: -0.127, maxima: 0.267, median: -0.018, bounds of box: -0.049 to 0.016, and bounds of whiskers: -0.147 to 0.113; LymEC: minima: -0.135, maxima: 0.188, median: -0.027, bounds of box: -0.056 to 0.008, and bounds of whiskers:-0.154 to 0.105; MEC: minima: -0.122, maxima: 0.141, median: -0.05, bounds of box: -0.074 to -0.023, and bounds of whiskers: -0.15 to 0.053), SLC transporters (**F,** 418 genes; CapEC: minima: -0.059, maxima: 0.096, median: 0.007, bounds of box: -0.004 to 0.019, and bounds of whiskers: -0.04 to 0.055; AEC: minima: -0.079, maxima: 0.069, median: -0.018, bounds of box: -0.034 to -0.002, and bounds of whiskers: -0.081 to 0.045; AngEC: minima: -0.078, maxima: 0.074, median: -0.014, bounds of box: -0.026 to 0.001, and bounds of whiskers: -0.067 to 0.041; VEC: minima: -0.066, maxima: 0.085, median: -0.001, bounds of box: -0.014 to 0.012, and bounds of whiskers: -0.053 to 0.051; LymEC: minima: -0.072, maxima: 0.059, median: -0.011, bounds of box: -0.024 to 0.003, and bounds of whiskers: -0.065 to 0.044; MEC: minima: -0.074, maxima: 0.061, median: -0.023, bounds of box: -0.037 to -0.009, and bounds of whiskers: -0.079 to 0.034), and tight junction proteins (**G,** 135 genes; CapEC: minima: -0.173, maxima: 0.325, median: 0.046, bounds of box: 0.003 to 0.093, and bounds of whiskers: -0.131 to 0.227; AEC: minima: -0.182, maxima: 0.324, median: 0.034, bounds of box: -0.017 to 0.084, and bounds of whiskers: -0.167 to 0.234; AngEC: minima: -0.199, maxima: 0.318, median: -0.018, bounds of box: -0.064 to 0.032, and bounds of whiskers: -0.208 to 0.175; VEC: minima: -0.194, maxima: 0.176, median: -0.051, bounds of box: -0.092 to -0.005, and bounds of whiskers: -0.222 to 0.125; LymEC: minima: -0.19, maxima: 0.238, median: -0.037, bounds of box: -0.084 to 0.016, and bounds of whiskers: -0.233 to 0.165; MEC: minima: -0.189, maxima: 0.284, median: -0.019, bounds of box: -0.064 to 0.035, and bounds of whiskers: -0.211 to 0.182) in CapECs. **H-J** Box plots validating the dynamic expression models during cerebrovascular development of ABC transporters (**H**, 49 genes; 3dpf: minima: -0.35, maxima: 1.387, median: 0.03, bounds of box: -0.154 to 0.236, and bounds of whiskers: -0.739 to 0.821; 6dpf: minima: -0.259, maxima: 1.496, median: 0.266, bounds of box: 0.08 to 0.473, and bounds of whiskers: -0.509 to 1.062; 11dpf: minima: -0.261, maxima: 1.654, median: 0.494, bounds of box: 0.306 to 0.704, and bounds of

whiskers: -0.291 to 1.302), SLC transporters (**I**, 418 genes; 3dpf: minima: -0.301, maxima: 1.155, median: 0.195, bounds of box: 0.044 to 0.341, and bounds of whiskers: -0.402 to 0.787;6dpf: minima: -0.301, maxima: 1.035, median: 0.363, bounds of box: 0.195 to 0.507, and bounds of whiskers: -0.272 to 0.974;11dpf: minima: -0.151, maxima: 0.977, median: 0.438, bounds of box: 0.29 to 0.589, and bounds of whiskers: -0.159 to 1.038), and tight junction proteins (**J**, 135 genes; 3dpf: minima: -0.463, maxima: 0.803, median: 0.081, bounds of box: -0.072 to 0.271, and bounds of whiskers: -0.587 to 0.786; 6dpf: minima: -0.458, maxima: 1.152, median: 0.217, bounds of box: 0.087 to 0.35, and bounds of whiskers: -0.307 to 0.744; 11dpf: minima: -0.401, maxima: 0.926, median: 0.211, bounds of box: 0.093 to 0.325, and bounds of whiskers: -0.255 to 0.673) in CapECs. Statistical significance was assessed using two-sided Student's *t*-test (**E-J**). Statistical significance is represented by ns: no-significant, *$p < 0.05$, **$p < 0.01$, ***$p < 0.001$.

Figure 3. Conservation of EC subtypes between zebrafish and mammals

A Specific function gene expression models of EC subtypes between zebrafish and mammals, the correlation value between zebrafish and mammals were listed under the species names. **B-D** Expression evaluation of gene modules including ABC transporters (**B,** mouse: 42 genes; E12.5: minima: -0.059, maxima: 0.14, median: 0.007, bounds of box: -0.013 to 0.017, and bounds of whiskers: -0.058 to 0.062; E13.5: minima: -0.062, maxima: 0.143, median: 0.003, bounds of box: -0.034 to 0.05, and bounds of whiskers: -0.159 to 0.174; E14.5: minima: -0.046, maxima: 0.175, median: 0.032, bounds of box: 0.003 to 0.04, and bounds of whiskers: -0.052 to 0.095; E15.5: minima: -0.048, maxima: 0.142, median: 0.041, bounds of box: 0.003 to 0.073, and bounds of whiskers: -0.102 to 0.178; E16.5: minima: -0.047, maxima: 0.148, median: 0.044, bounds of box: 0.011 to 0.095, and bounds of whiskers: -0.115 to 0.221; E17.5: minima: -0.078, maxima: 0.195, median: 0.053, bounds of box: 0.012 to 0.072, and bounds of whiskers: -0.078 to 0.162; human: 44 genes; GW9: minima: -0.151, maxima: 0.091, median: -0.045, bounds of box: -0.07 to -0.019, and bounds of whiskers: -0.145 to 0.057; GW14.4-16.4: minima: -0.175, maxima: 0.23, median: 0.01, bounds of box: -0.022 to 0.049, and bounds of whiskers: -0.13 to 0.156; GW15: minima: -0.156, maxima: 0.227, median: 0.012, bounds of box: -0.024 to 0.051, and bounds of whiskers: -

0.137 to 0.165; GW18: minima: -0.148, maxima: 0.272, median: 0.003, bounds of box: -0.042 to 0.046, and bounds of whiskers: -0.175 to 0.179), SLC transporters (**C,** mouse: 290 genes; E12.5: minima: -0.025, maxima: 0.05, median: 0.006, bounds of box: -0.011 to 0.024, and bounds of whiskers: -0.065 to 0.078; E13.5: minima: -0.031, maxima: 0.09, median: 0.002, bounds of box: -0.009 to 0.026, and bounds of whiskers: -0.062 to 0.078; E14.5: minima: -0.031, maxima: 0.099, median: 0.013, bounds of box: 0.001 to 0.023, and bounds of whiskers: -0.03 to 0.055; E15.5: minima: -0.006, maxima: 0.097, median: 0.027, bounds of box: 0.021 to 0.049, and bounds of whiskers: -0.021 to 0.091; E16.5: minima: -0.003, maxima: 0.077, median: 0.025, bounds of box: 0.012 to 0.051, and bounds of whiskers: -0.045 to 0.109; E17.5: minima: -0.025, maxima: 0.082, median: 0.04, bounds of box: 0.024 to 0.047, and bounds of whiskers: -0.011 to 0.082; human: 245 genes; GW9: minima: -0.073, maxima: 0.029, median: -0.028, bounds of box: -0.043 to -0.014, and bounds of whiskers: -0.087 to 0.029; GW14.4-16.4: minima: -0.079, maxima: 0.099, median: -0.016, bounds of box: -0.032 to 0.002, and bounds of whiskers: -0.082 to 0.052; GW15: minima: -0.126, maxima: 0.111, median: 0.013, bounds of box: -0.008 to 0.035, and bounds of whiskers: -0.072 to 0.099; GW18: minima: -0.09, maxima: 0.117, median: 0.008, bounds of box: -0.013 to 0.031, and bounds of whiskers: -0.078 to 0.097), and tight junction proteins (**D,** mouse: 131 genes; E12.5: minima: 0.001, maxima: 0.193, median: 0.129, bounds of box: 0.041 to 0.17, and bounds of whiskers: -0.151 to 0.362; E13.5: minima: -0.02, maxima: 0.199, median: 0.101, bounds of box: 0.054 to 0.148, and bounds of whiskers: -0.088 to 0.29; E14.5: minima: 0.01, maxima: 0.221, median: 0.116, bounds of box: 0.057 to 0.187, and bounds of whiskers: -0.137 to 0.382; E15.5: minima: 0.055, maxima: 0.386, median: 0.187, bounds of box: 0.155 to 0.238, and bounds of whiskers: 0.031 to 0.362; E16.5: minima: 0.105, maxima: 0.272, median: 0.189, bounds of box: 0.153 to 0.226, and bounds of whiskers: 0.044 to 0.336; E17.5: minima: 0.117, maxima: 0.275, median: 0.186, bounds of box: 0.15 to 0.216, and bounds of whiskers: 0.051 to 0.315; human: 132 genes; GW9: minima: -0.027, maxima: 0.305, median: 0.11, bounds of box: 0.079 to 0.157, and bounds of whiskers: -0.039 to 0.275; GW14.4-16.4: minima: -0.052, maxima: 0.468, median: 0.199, bounds of box: 0.146 to 0.254, and bounds of whiskers: -0.017 to 0.417; GW15: minima: -

0.235, maxima: 0.533, median: 0.156, bounds of box: 0.107 to 0.208, and bounds of whiskers: -0.044 to 0.359; GW18: minima: -0.043, maxima: 0.499, median: 0.194, bounds of box: 0.135 to 0.251, and bounds of whiskers: -0.039 to 0.425) during cerebrovascular development between mouse and human. Statistical significance was assessed using two-sided Student's *t*-test (**B-D**). Statistical significance is represented by ns: no-significant, $*p < 0.05$, $**p < 0.01$, $***p < 0.001$.

Figure 4. Mapping of different EC types in cerebrovascular network based on IISS during zebrafish development

A IISS signals of 36 genes on the continuous brain sections of zebrafish at 3, 6, and 11 dpf (thickness = 10 μm). **B** Representative examples of gene and cellular localization within vascular networks in IISS. Colored curves/circles: blood vessels; Colored polygon: cells; colored dots: genes (refer to the color coding in A). Scale bars: 100 μm (left and middle) and 10 μm (right). **C** Distribution proportions of different EC types across the zebrafish cerebrovascular subnetworks. **D** Spatiotemporal density gradients for CapECs, AECs, VECs, and AngECs. Colors encode the cell density normalized to the population size of the corresponding EC type. Scale bars: 100 μm. **E** Heatmaps display the density of CapECs, AECs, VECs, and AngECs in different blood vessels across 3, 6, and 11 dpf**.** Red highlights progressively specialized vessels in mesencephalon and metencephalon, and blue highlights the lateral vessels undergoing gradual de-specialization.

Figure 5. The influence of genes represented by *zgc:158423* and *slc16a1a* on cerebrovascular development

A-B Density distribution of s*lc16a1a*$^+$ ECs and *zgc:158423*$^+$ ECs in zebrafish cerebrovasculature. Heatmaps: colors represent the cell density normalized to the population size of the corresponding EC type. Scale bars: 100 μm. **C** Represent images of 3 dpf zebrafish brain vasculature and their construction for control, *slc16a1a*, *zgc:158423* and *cldc1* crispants. Scale bars: 100 μm. **D-E** Statistics on the length of the whole cerebrovasculature (**D**) and different types of vasculatures (**E**) in 3 dpf zebrafish. N (control) = 6, n (*slc16a1a*) = 6, n (*zgc:158423*) = 7, n (*cldc1*) = 6. **F, G** Statistics on the total number of vascular segments (**F**) and the number of various vascular

segments (**G**) in 3 dpf zebrafish. N (control) = 6, n (*slc16a1a*) = 6, n (*zgc:158423*) = 7, n (*cldc1*) = 6. Data were presented as mean ± SEM. **H**. Representative images of zebrafish cerebrovascular permeability in 3 dpf control, *slc16a1a*, *zgc:158423*, and *cldc1* crispants. Evans Blue leakage is indicated by yellow arrows. Scale bar: 100 μm. N (Control) = 11, n (*slc16a1a*) = 14, n (*zgc:158423*) = 16 and n (*cldc1*) = 13. **I.** Quantification of whole-brain BBB permeability (leakage points) for the groups shown in (**H**) at 3 dpf (Control: minima: 0.38, maxima: 1.71, median: 0.91, bounds of box: 0.71 to 1.36, bounds of whiskers: -0.25 to 2.32; *slc16a1a* crispant: minima: 2.76, maxima: 5.71, median: 3.76, bounds of box: 3.5 to 3.9, bounds of whiskers: 2.9 to 4.5; *zgc:158423* crispant: minima: 1.14, maxima: 2.86, median: 1.91, bounds of box: 1.69 to 2.55, bounds of whiskers: 0.39 to 3.84; *cldc1* crispant: minima: 0.57, maxima: 1.62, median: 0.86, bounds of box: 0.76 to 0.95, bounds of whiskers: 0.48 to 1.24). **J.** Representative images of zebrafish cerebrovascular permeability in 6 dpf control, *slc16a1a*, *zgc:158423*, and *cldc1* crispants. Evans Blue leakage is indicated by yellow arrows. Scale bar: 100 μm. N (Control) = 13, n (*slc16a1a*) = 9, n (*zgc:158423*) = 10 and n (*cldc1*) = 12. **K.** Quantification of whole-brain BBB permeability (leakage points) for the groups shown in (**J**) at 6 dpf (Control: minima: 0.6, maxima: 1.74, median: 1.04, bounds of box: 0.69 to 1.14, bounds of whiskers: 0.02 to 1.82; *slc16a1a* crispant: minima: 1.24, maxima: 2.43, median: 1.69, bounds of box: 1.44 to 1.84, bounds of whiskers: 0.84 to 2.44; *zgc:158423* crispant: minima: 1.19, maxima: 2.03, median: 1.54, bounds of box: 1.38 to 1.65, bounds of whiskers: 0.97 to 2.07; *cldc1* crispant: minima: 0.65, maxima: 1.69, median: 1.07, bounds of box: 0.98 to 1.29, bounds of whiskers: 0.51 to 1.76). Statistical significance was assessed using two-sided Student's *t*-test (E-G, I and K). Statistical significance is represented by ns: no-significant, $*p < 0.05$, $**p < 0.01$, $***p < 0.001$.

Editor Summary

This study maps a spatiotemporal atlas of zebrafish cerebrovascular development, linking genes and cells to 3D vascular architecture. It reveals how vessel networks form and identifies key genes essential for blood-brain barrier integrity.

Peer review information: *Nature Communications* thanks Saulius Sumanas and the other, anonymous, reviewer(s) for their contribution to the peer review of this work. A peer review file is available.

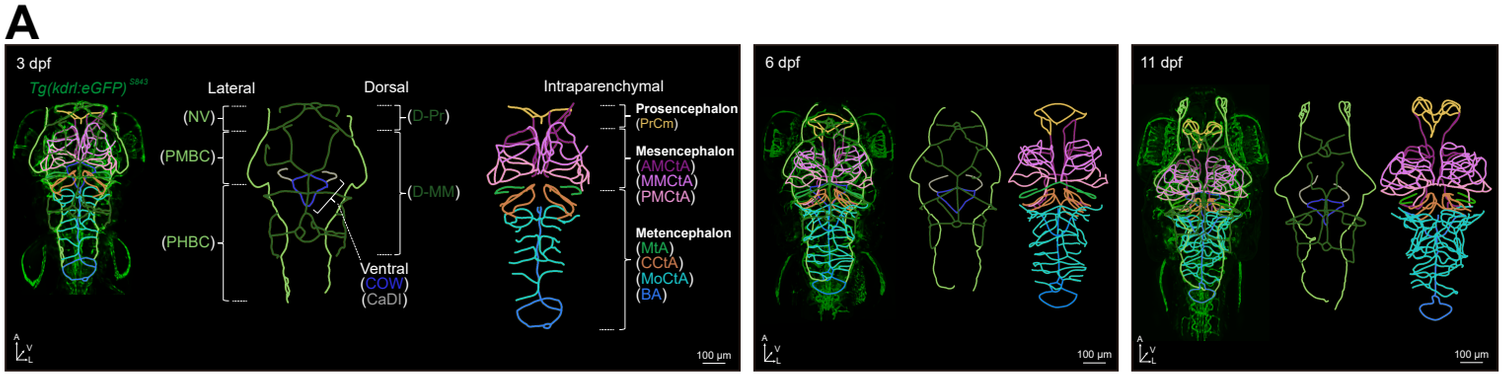

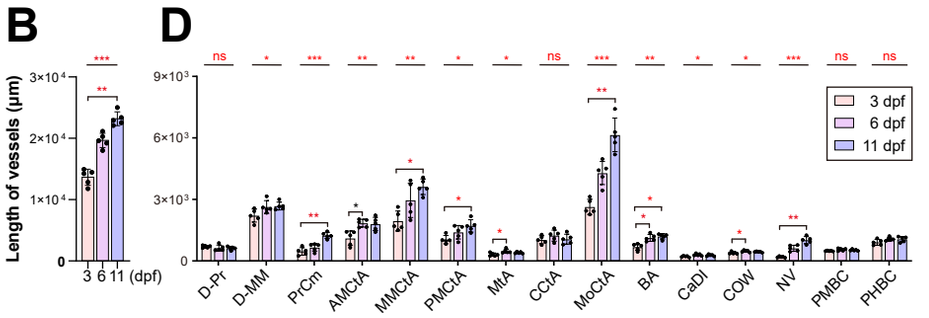

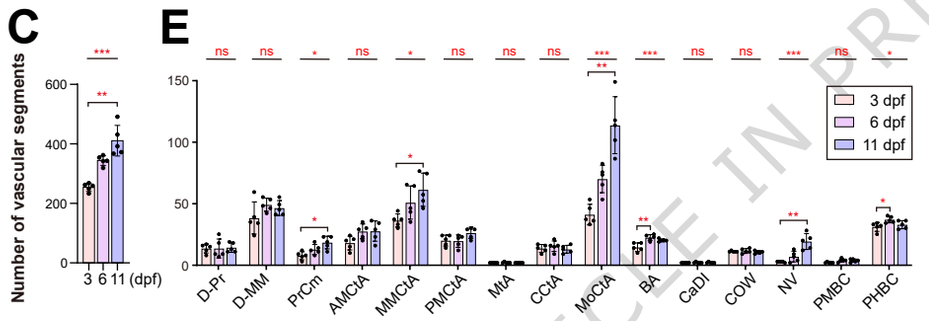

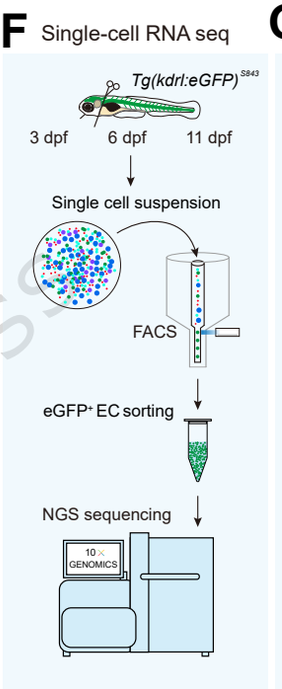

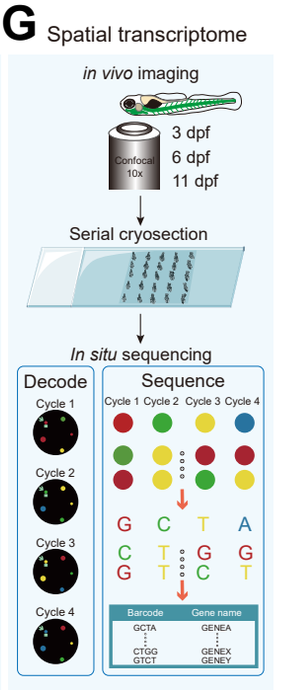

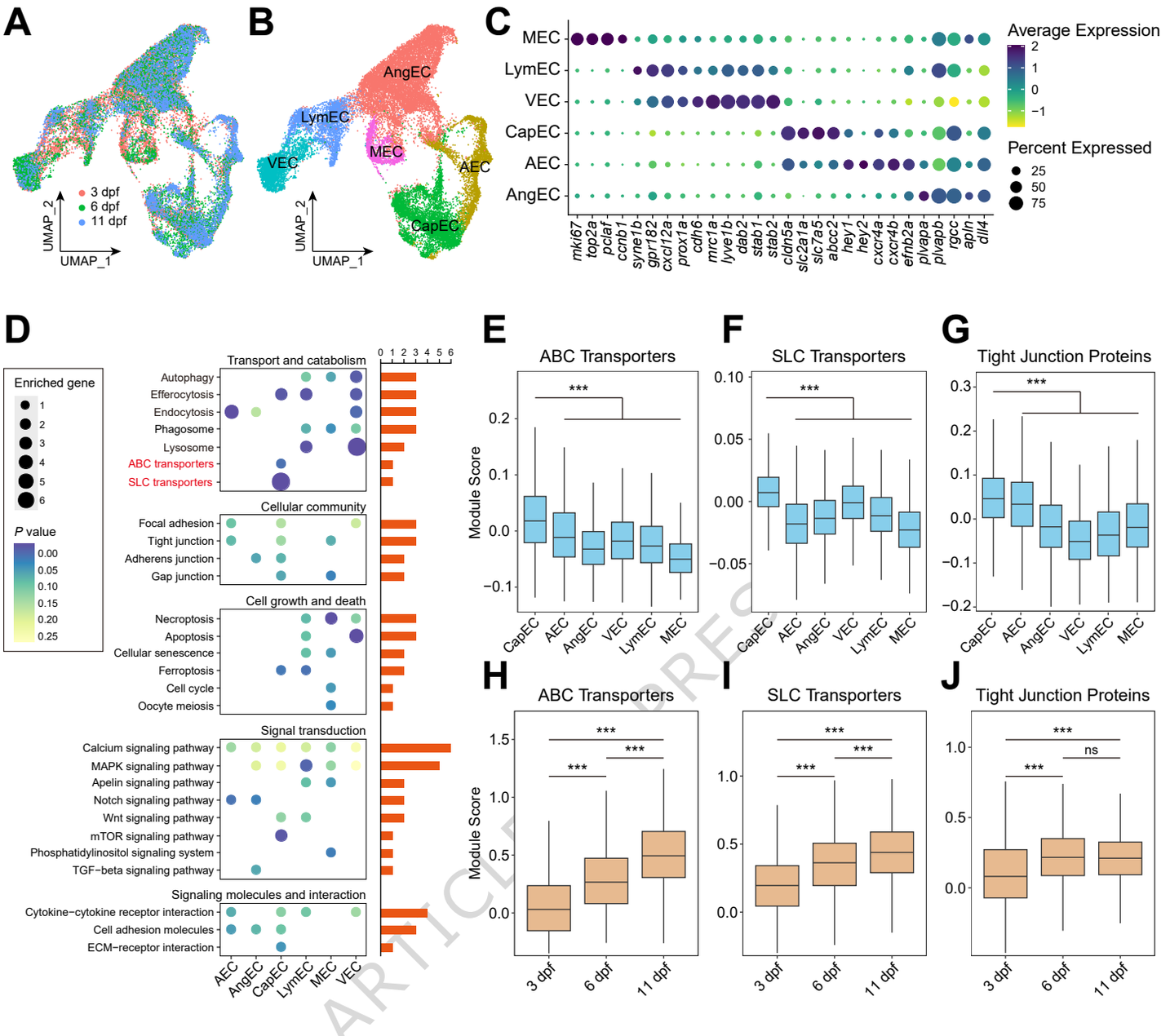

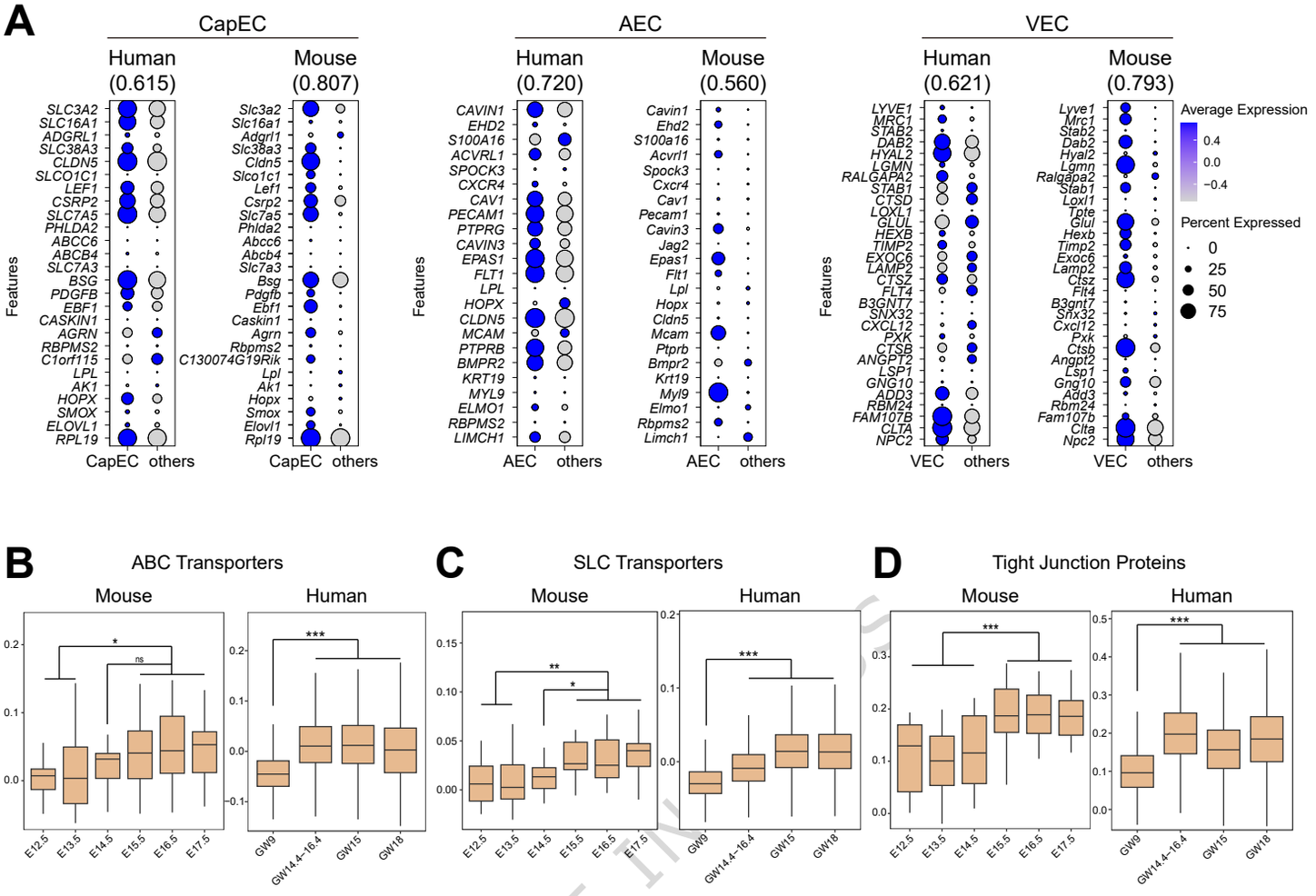

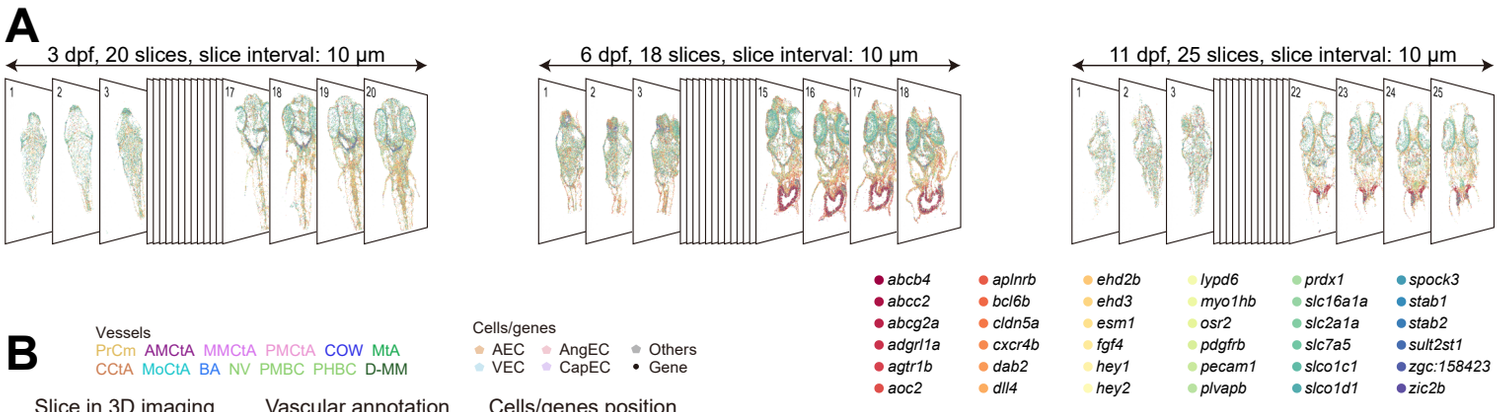
A
3 dpf, 20 slices, slice interval: 10 μm
6 dpf, 18 slices, slice interval: 10 μm
11 dpf, 25 slices, slice interval: 10 μm
abcb4 abcc2 abcg2a adgrl1a agtr1b aoc2
aplnrb bcl6b cldn5a cxcr4b dab2 dll4
ehd2b ehd3 esm1 fgf4 hey1 hey2
lypd6 myo1hb osr2 pdgfrb pecam1 plvapb
prdx1 slc16a1a slc2a1a slc7a5 slco1c1 slco1d1
spock3 stab1 stab2 sult2st1 zgc:158423 zic2b

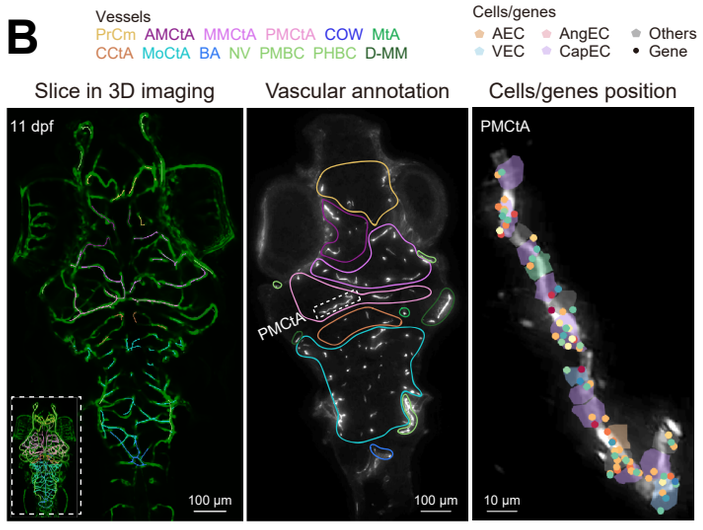
B
Vessels
PrCm AMCtA MMCtA PMCtA COW MtA
CCtA MoCtA BA NV PMBC PHBC D-MM
Cells/genes
AEC AngEC Others
VEC CapEC Gene
Slice in 3D imaging
Vascular annotation
Cells/genes position
11 dpf
PMCtA
100 μm
100 μm
10 μm

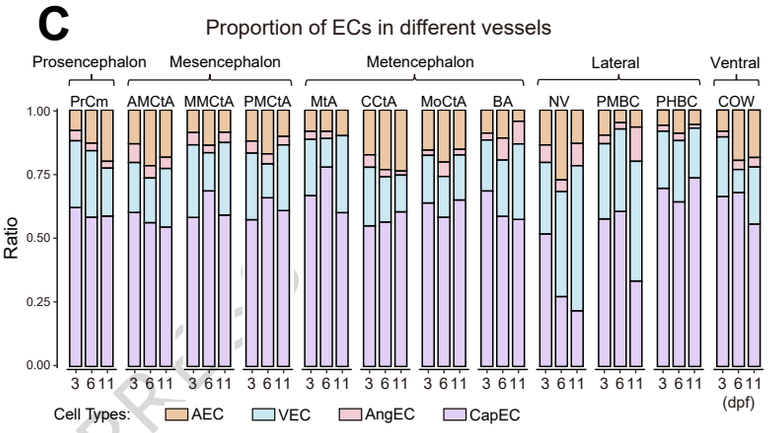
C
Proportion of ECs in different vessels
Prosencephalon
Mesencephalon
Metencephalon
Lateral
Ventral
PrCm AMCtA MMCtA PMCtA MtA CCtA MoCtA BA NV PMBC PHBC COW
Ratio
1.00
0.75
0.50
0.25
0.00
3 6 11
(dpf)
Cell Types: AEC VEC AngEC CapEC

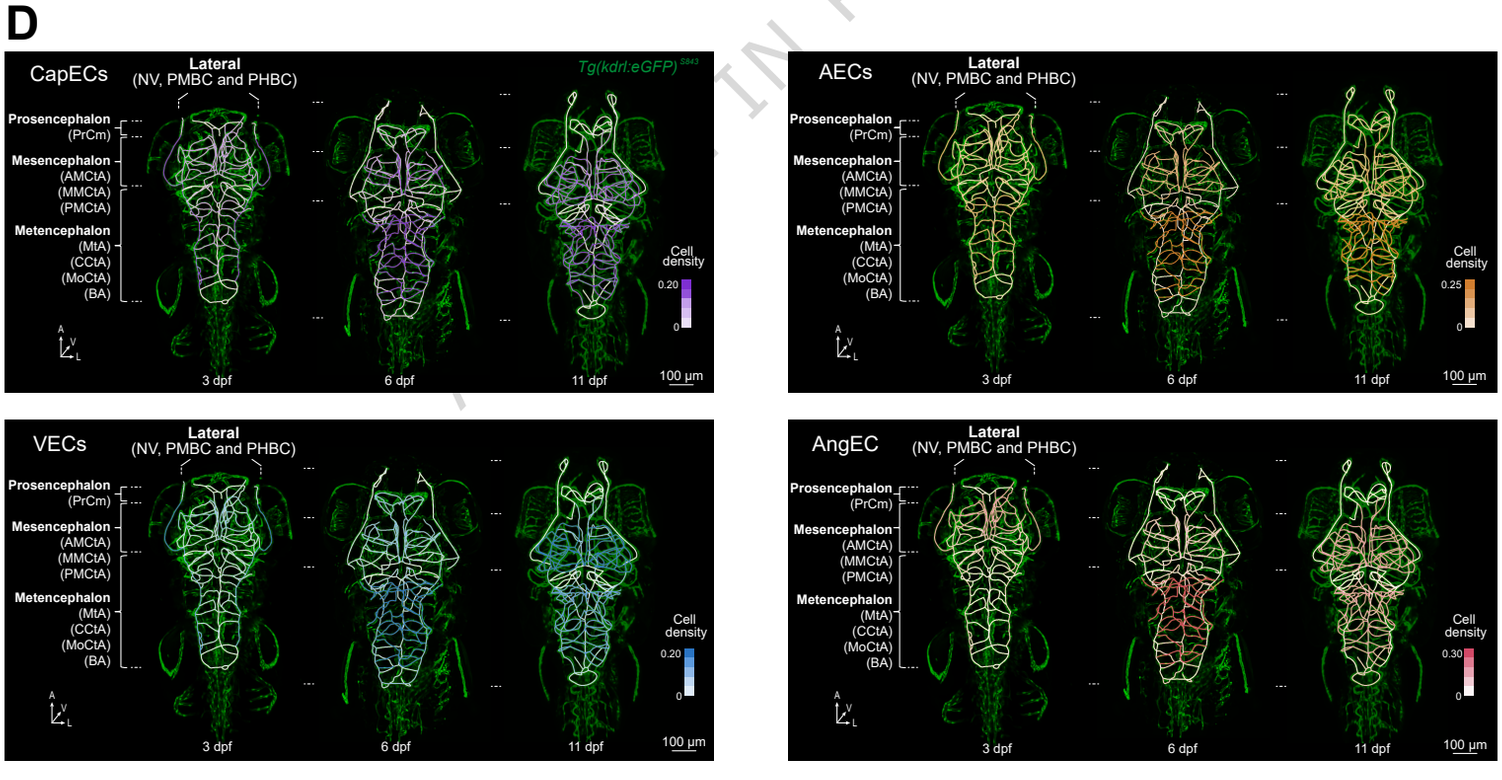
D
CapECs
AECs
VECs
AngEC
Lateral
(NV, PMBC and PHBC)
Tg(kdrl:eGFP)
Prosencephalon
(PrCm)
Mesencephalon
(AMCtA)
(MMCtA)
(PMCtA)
Metencephalon
(MtA)
(CCtA)
(MoCtA)
(BA)
Cell density
3 dpf
6 dpf
11 dpf
100 μm

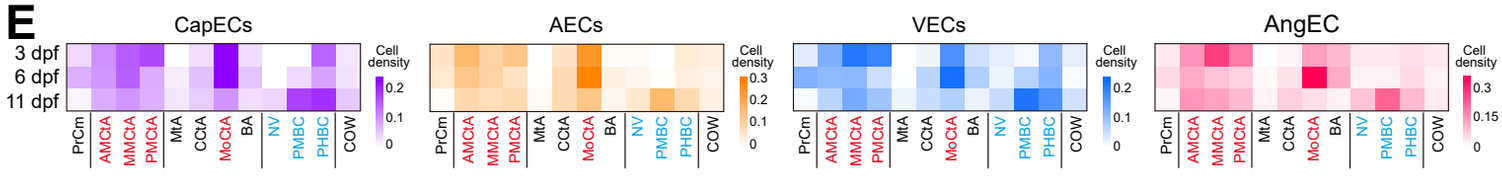
E
CapECs
AECs
VECs
AngEC
3 dpf
6 dpf
11 dpf
PrCm AMCtA MMCtA PMCtA MtA CCtA MoCtA BA NV PMBC PHBC COW
Cell density

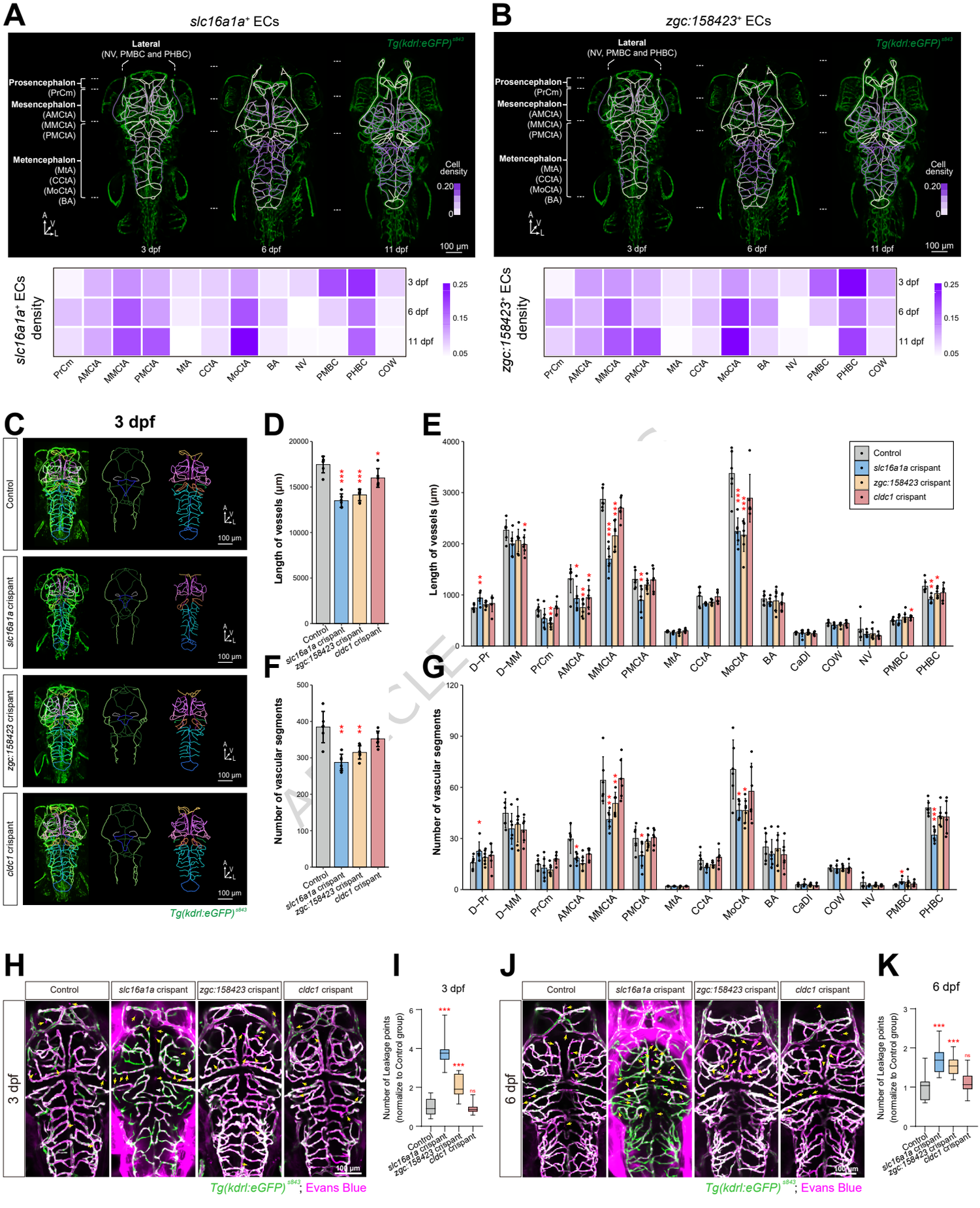
A
slc16a1a+ ECs
Lateral
(NV, PMBC and PHBC)
Tg(kdrl:eGFP)s843
Prosencephalon
(PrCm)
Mesencephalon
(AMCtA)
(MMCtA)
(PMCtA)
Metencephalon
(MtA)
(CCtA)
(MoCtA)
(BA)
Cell density
0.20
0
3 dpf
6 dpf
11 dpf
100 µm
slc16a1a+ ECs density
0.25
0.15
0.05
PrCm
AMCtA
MMCtA
PMCtA
MtA
CCtA
MoCtA
BA
NV
PMBC
PHBC
COW
B
zgc:158423+ ECs
zgc:158423+ ECs density
C
3 dpf
Control
slc16a1a crispant
zgc:158423 crispant
cldc1 crispant
Tg(kdrl:eGFP)s843
D
Length of vessels (µm)
E
Length of vessels (µm)
Control
slc16a1a crispant
zgc:158423 crispant
cldc1 crispant
D-Pr
D-MM
CaDI
F
Number of vascular segments
G
Number of vascular segments
H
3 dpf
Tg(kdrl:eGFP)s843; Evans Blue
I
3 dpf
Number of Leakage points
(normalize to Control group)
J
6 dpf
Tg(kdrl:eGFP)s843; Evans Blue
K
6 dpf
Number of Leakage points
(normalize to Control group)